Title

Chaotrope-Based Approach for Rapid In Vitro Assembly and Loading of Bacterial Microcompartment Shells

Permalink

https://escholarship.org/uc/item/0b2188qm

Journal

ACS Nano, 19(12)

ISSN

1936-0851

Authors

Range, Kyleigh L
Chiang, Timothy K
Pramanik, Arinita
et al.

Publication Date

2025-04-01

DOI

10.1021/acsnano.4c15538

Copyright Information

ACS NANO

www.acsnano.org

Chaotrope-Based Approach for Rapid In Vitro Assembly and Loading of Bacterial Microcompartment Shells

Kyleigh L. Range,◆ Timothy K. Chiang,◆ Arinita Pramanik, Joel F. Landa, Samuel N. Snyder, Xiaobing Zuo, David M. Tiede, Lisa M. Utschig, Eric L. Hegg, Markus Sutter,* Cheryl A. Kerfeld,* and Corie Y. Ralston

Cite This: *ACS Nano* 2025, 19, 11913−11923

ABSTRACT: Bacterial microcompartments (BMCs) are proteinaceous organelles that self-assemble into selectively permeable shells that encapsulate enzymatic cargo. BMCs enhance catalytic pathways by reducing crosstalk among metabolites, preventing harmful intermediates from leaking into the cytosol and increasing reaction efficiency via enzyme colocalization. The intrinsic properties of BMCs make them attractive for biotechnological engineering. However, in vivo expression methods for shell synthesis have significant drawbacks that limit the potential design space for these nanocompartments. Here, we describe the development of an efficient and rapid method for the in vitro assembly of BMC shells from their protein building blocks. Our method enables large-scale construction of BMC shells by utilizing urea as a chaotropic agent to control self-assembly and provides an approach for encapsulation of both biotic and abiotic cargo under a broad range of reaction conditions. We demonstrate an enhanced level of control over the assembly of BMC shells in vitro and expand the design parameter space for engineering BMC systems with specialized and enhanced catalytic properties.

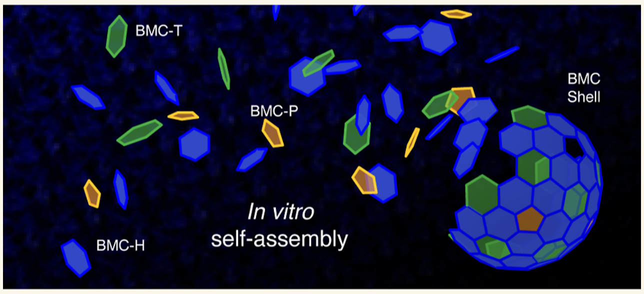

KEYWORDS: *bacterial microcompartments, in vitro, self-assembly, urea, biotic and abiotic cargo encapsulation, catalysis, confinement*

INTRODUCTION

Membrane-bound organelles were once thought to be an exclusive characteristic of eukaryotes, but partitioned structures in bacteria also provide a wide diversity of subcellular organizational systems across domains. In contrast to lipid membrane-bound eukaryotic organelles, bacterial microcompartments (BMCs) use only proteins[1,2] to encapsulate various metabolic pathways.[7] The carboxysome, for example, is a BMC that is found among cyanobacteria and other autotrophic bacteria that enhances carbon fixation through colocalization of the enzyme RuBisCO (ribulose-1,5-biphosphate carboxylase/oxygenase) and concentrating its substrate, CO2, thereby overcoming some of RuBisCO's inefficiencies.[4,5] By encapsulating catalysts within a selectively permeable protein membrane, BMC shells increase enzyme efficiency through colocalization, prevent metabolic crosstalk between competing substrates, and eliminate the spillage of toxic or volatile intermediates into the cytosol.[3,6] The polyhedral BMC shell is composed of hexameric, pseudohexameric, and pentameric "tiles" that are evolutionarily conserved across different taxa. In BMCs, the most abundant shell tiles, hexamers, consist of six identical protomers containing a single pfam00936 domain (BMC-H proteins). BMC-T proteins, a fusion of two copies of the pfam00936 domain, form trimers that resemble the hexamers in size and shape and are a less abundant component of shell facets.[1,2] Pentamers (BMC-P proteins) that cap the vertices of the polyhedral shell are composed of five protomers of the pfam03319 domain.[7]

Since the first report of a recombinantly expressed BMC system,[8] purification and characterization of native BMCs[9−12] and empty shells[13−18] has contributed to an increased understanding of the shell structure, function, and assembly. Although its native function is unknown, the microcompart-

Received: October 31, 2024
Revised: March 10, 2025
Accepted: March 12, 2025
Published: March 20, 2025

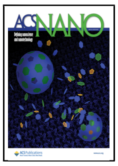

https://doi.org/10.1021/acsnano.4c15538

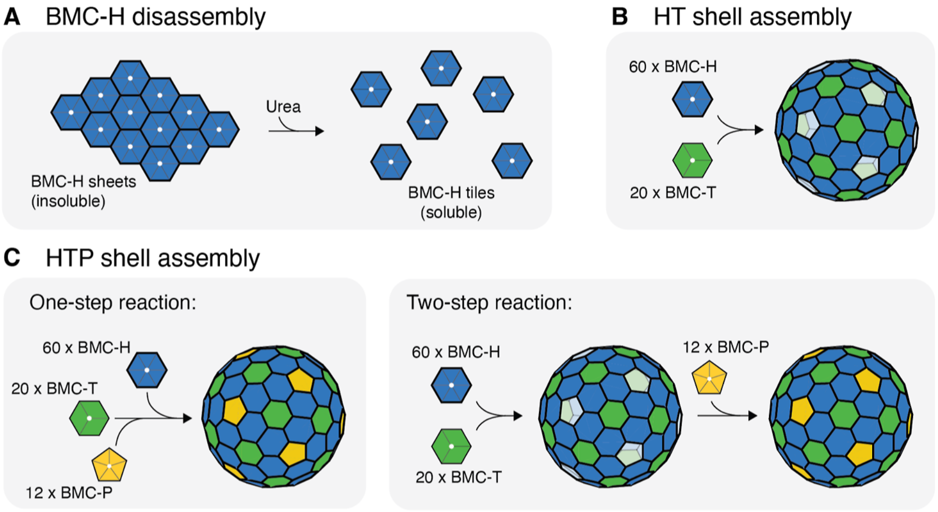

Figure 1. Schematic representation of the chaotrope-based approach to *in vitro* BMC shell assembly. (A). BMC-H hexamers form sheets that disassemble into assembly competent tiles upon the addition of urea. (B). Combining solutions of heterologously expressed and purified BMC-H and BMC-T shell proteins results in the IVA of HT shells. (C). Combining solutions of all three BMC shell proteins results in the IVA of HTP shells. HTP shells can be assembled upon mixing via a one-step (BMC-H + BMC-T + BMC-P) or two-step (BMC-H + BMC-T first, then BMC-P) addition.

ment from*Haliangium ochraceum* (HO) provides robust *in vivo* shell assembly through recombinant expression of its shell protein constituents.[19] Through manipulation of a synthetic operon, three main shell types (full, minimal, and minimal wiffle shells) can be purified from heterologous expression.[20] Full HO shells incorporate three distinct trimer proteins, of which two (BMC-T2 and BMC-T3) form dimers of trimers that are double-layered. Minimal (HTP) and minimal wiffle (HT) HO shells both contain only a single type of trimer (BMC-T1, referred to here onward as BMC-T) with BMC-H arranged in $T = 9$ icosahedra, differing in that minimal wiffle shells lack pentamers at the 12 icosahedral vertices. The stoichiometric ratio of shell tiles in a minimal HTP shell is 60:20:12 BMC-H:BMC-T:BMC-P or 60:20 BMC-H:BMC-T in a minimal wiffle HT shell.[21]

In vivo expression and purification of BMC shells do not provide precise control of shell composition in self-assembly. Furthermore, it is time- and labor-intensive, requiring the design of multiple variations of a fundamental synthetic operon, rounds of cloning, and subsequent characterization screenings to ensure successful shell assembly. Moreover, shells expressed *in vivo* adventitiously capture unwanted contaminants from the cytosolic milieu.[22] Previously, an *in vitro* assembly (IVA) method for constructing BMC shells was reported that overcame several limitations of recombinantly expressed shells, offering a higher degree of control over shape, size, and cargo content.[23] This method relied on enzymatic activity to cleave a genetically introduced blocking group on BMC-H to initiate shell assembly; this inherently limits reaction conditions to the narrow range that is conducive to the enzymatic function. We have developed a chaotrope-based method for IVA of BMC shells. This method provides a powerful new tool for bioengineering efforts as it allows more precise control of shell composition, significantly increases both speed and efficiency, and expands the range of reaction conditions for assembly. Additionally, it provides increased flexibility in the choice of BMC tile building blocks, enabling a broader range of shell functionalization for a spectrum of significant applications such as drug delivery vehicles and bioengineered nanoreactors, facilitating controlled catalysis within these partitioned systems.

RESULTS

IVA of BMC Shells from Their Constituent Protein Tiles. We prepared purified shell proteins and combined them according to the reaction schemes shown in Figure 1. Complete sequences of all proteins used in this study are given in Table S1, and their molecular weights are given in Table S2. BMC-T and BMC-P tiles were heterologously expressed in *E. coli* and purified using affinity chromatography and were either dialyzed into Tris buffer or subjected to size exclusion chromatography (SEC). When HO BMC-H is heterologously expressed in*E. coli* in the absence of other shell proteins, it forms inclusion bodies that can be purified as a suspension of BMC-H sheets[24,25] (Figure 1A). These supramolecular sheet structures are insoluble, and the constituent BMC-H tiles are, therefore, not viable for assembling BMC shells. We obtained assembly competent BMC-H tiles in the soluble form by disassembling sheets with 500 mM urea (Figure 1A). We found that this urea concentration is high enough to disrupt BMC-H−BMC-H interactions within sheets, solubilizing BMC-H tiles without further denaturing the homohexamer subunit. The solubilized BMC-H, BMC-T, and BMC-P tiles were pure and monodisperse, as determined by dynamic light scattering (DLS) and SEC (Figure S1).

BMC shells were assembled by mixing purified solutions of BMC tiles according to the assembly reaction schemes shown in Figure 1B,C. To assemble HT or HTP shells, we combined BMC-T and BMC-P in Tris buffer before adding BMC-H with vigorous mixing, resulting in a rapid dilution of urea, followed by incubation at 4 °C for 24 h, mirroring the protocol from Hagen et al.[23] We also tested assembly after 2 min and 1 h to observe how assembly duration affects reaction efficiency. The HT shell assembly reactions were performed at 1 mg/mL BMC-H and 0.33 mg/mL BMC-T, following the expected stoichiometric molar ratio for an HT wiffle shell (3:1 BMC-H:BMC-T). The addition of pentamers in the HTP shell

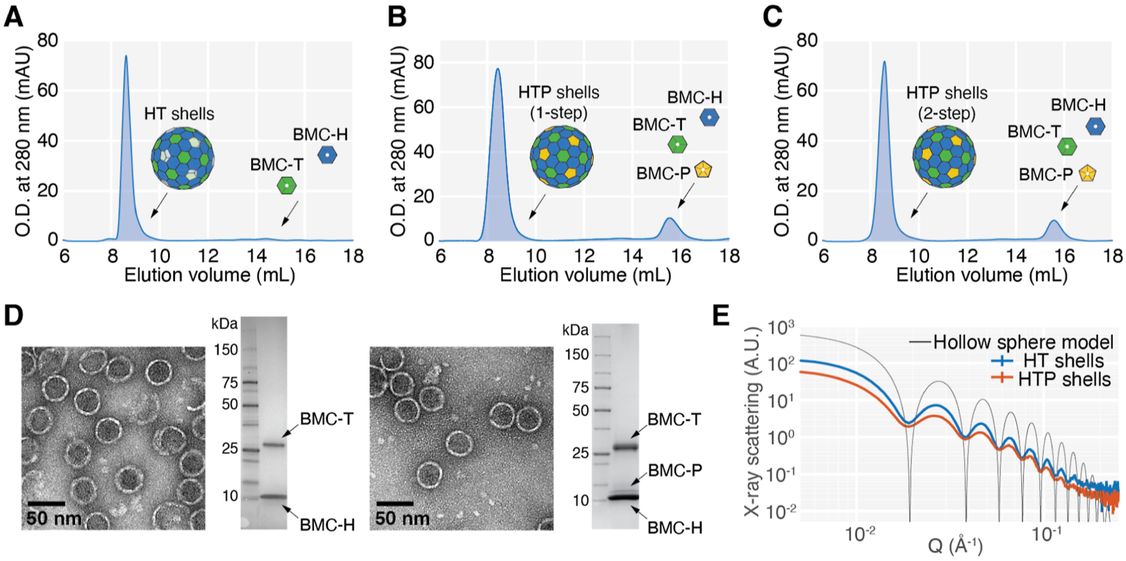

Figure 2. Characterization of *in vitro* assembled HT and HTP shells. (A). SEC chromatogram for *in vitro* assembled HT shells. The main elution peak contains monodisperse 40 nm hollow spheres made from BMC-H and BMC-T. (B−C). SEC chromatograms for *in vitro* HTP shells assembled via 1-step (B) and 2-step (C) reactions, with a 5-fold stoichiometric excess amount of BMC-P. The main elution peak contains monodisperse 40 nm hollow spheres made from BMC-H, BMC-T, and BMC-P. (D). Negative stain TEM micrographs and SDS-PAGE analyses of HT shells (left) and 1-step HTP shells (right). (E). SAXS spectra for *in vitro* assembled HT and HTP shells and simulated spectrum for a hollow sphere model with an inner radius of 150.5 Å and a shell thickness of 25 Å.

assembly reaction fills the 12 vacancies of HT shell vertices and creates a microenvironment within the shell that is essentially sealed from entry and exit of large solutes. We assembled HTP shells using a one-step or two-step protocol (Figure 1C). For the one-step HTP assemblies, we combined all three shell proteins in the IVA reaction with BMC-P in a 5-fold excess; 0.33 mg/mL BMC-T and 1 mg/mL BMC-P tiles were mixed into assembly buffer before the addition of 1 mg/mL BMC-H. We found that the soluble BMC-H tiles reassociate into insoluble sheets when the urea is diluted; therefore, in order to not prematurely dilute the urea before the initiation of shell assembly, it was the last component to be added to the reaction mixture. The reaction was similarly left to incubate at 4 °C. For the two-step assembly, we first generated minimal wiffle shells that were then capped with BMC-P, a method previously shown successful for *in vivo* generated HO shells.[20] We used the same conditions as in a recent report by Snyder et al.[26] and assembled verified HT shells before adding a 5-fold excess of BMC-P for a 30 min incubation period.

Characterization of Assembled Shell Components and Structure. To verify the formation of BMC shells, we analyzed the components and structure of the assemblies using sodium dodecyl sulfate polyacrylamide gel electrophoresis (SDS-PAGE), DLS, negative stain transmission electron microscopy (TEM), and small-angle X-ray scattering (SAXS). The assembled shells were purified using SEC and separated from individual tiles, and residual urea was removed (Figure 2A−C). In all assembly reactions, most of the protein eluted in the column void volume, indicating the presence of large assemblies. The size of the species in these fractions were measured to be approximately 40 nm with low polydispersity, as determined by DLS (Figure S1), which is consistent with previously reported HO BMC shell diameters.[19,21,27] Direct imaging using negative stain TEM analysis of the shell fractions provided confirmation of assembled shell structures, and SDS-PAGE analysis verified the composition of the shells (Figure 2D). Shell assemblies were also characterized with SAXS to verify the assembly size and structure. The SAXS profiles depict oscillatory features that reflect the core−shell particle structures (Figure 2E). The attenuation of the oscillations in the experimental data, compared to the model SAXS spectrum, is due in part to the polyhedral structure of the shell, which deviates from an ideal sphere. In comparison with HTP shells assembled *in vivo* (Figure S2), the SAXS profiles of the *in vitro* assembled HTP shells exhibit slightly more attenuation of the oscillatory features and a shift in the first minimum/maximum oscillation to a lower Q value, suggesting a broader size distribution in the *in vitro* assembled sample. TEM images of HT shells suggest that this polydispersity may arise from the assembly of polymorphic structures, such as elongated shells that are reminiscent of prolate bacteriophage capsids[28] (Figure S3) and that have been previously observed in recombinant BMC shells.[29,30] Nonetheless, comparison of the *in vitro* assembled HT and HTP shells with *in vivo* expressed HTP shells and modeled hollow core−shell spheres illustrates consistency across all structures.

***In Vitro* Shell Assembly Reaction Efficiency and Speed.** We next sought to quantify the efficiency and speed of the assembly. We define assembly efficiency as the amount of protein in the shell form as a fraction of the total amount of protein in both the shell form and unassembled tiles. We determined the amount of protein from the SEC fractions by integrating the UV 280 absorbance peaks. Because the scattering contributions from the large assembled shells are non-negligible, these measurements were also compared to the results from a BCA assay (Figure S4). In assemblies that utilize the expected stoichiometry of tiles, we find that assembly efficiency reliably reaches between 75 and 94% (Figures 3A, S4 and S5). This is significantly higher than that from the previous IVA method,[23] which reported an approximate efficiency of 20%. Moreover, since the previous IVA method relied on an enzymatic cleavage step, maximum assembly efficiency was achieved only for overnight incubations.

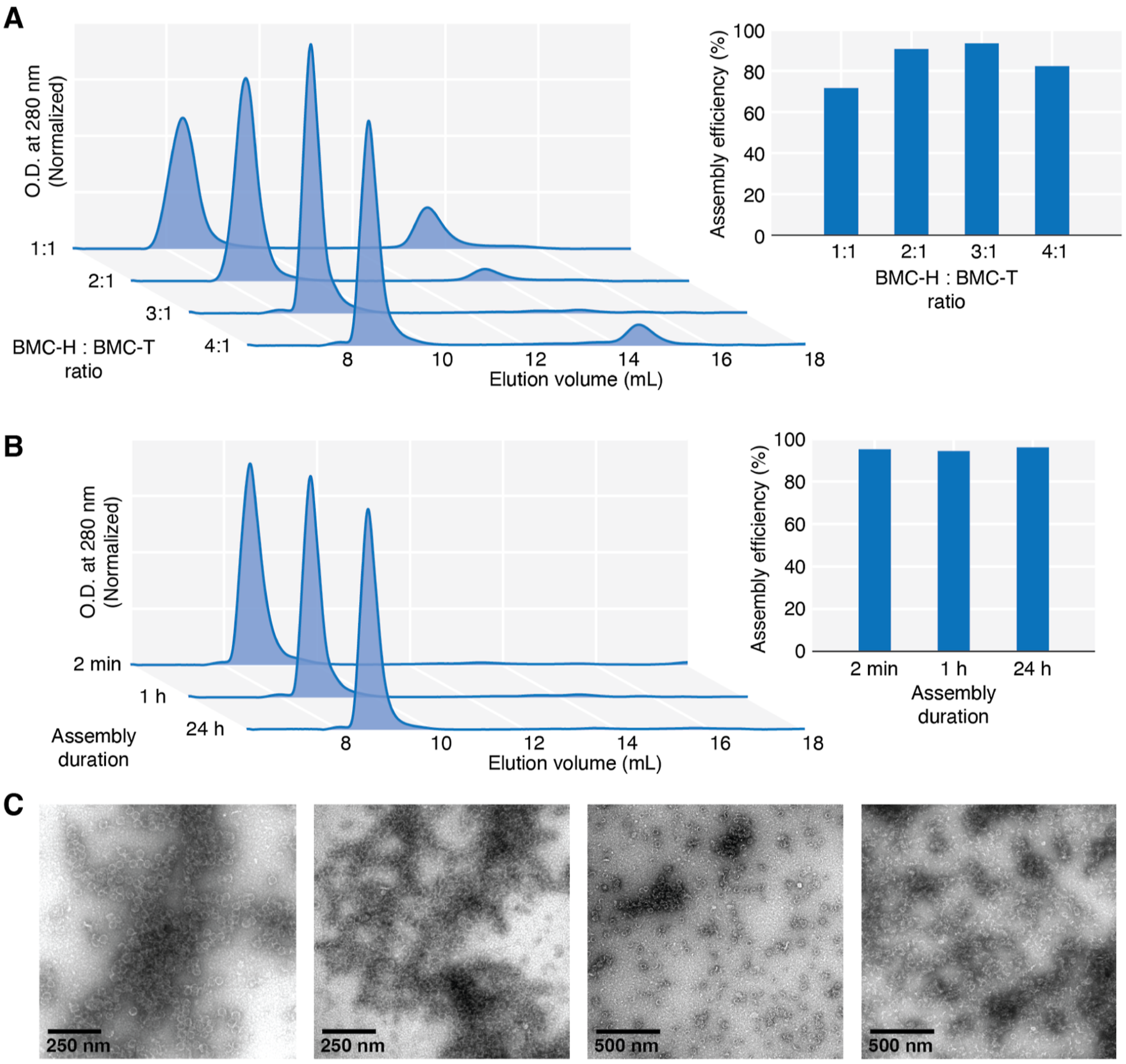

Figure 3. IVA of HT shells is efficient and fast. (A). SEC chromatograms of HT shell assembly reactions containing varying BMC-H:BMC-T stoichiometries. The bar graph shows that the assembly efficiency is highest at the expected stoichiometric ratio of 3:1 BMC-H to BMC-T. Efficiency is defined as the area of the chromatogram peak containing shells divided by the total area. (B). SEC chromatograms of HT shells assembled with varying duration at a fixed BMC-H:BMC-T ratio of 3:1. The bar graph shows that the reaction efficiencies among 2 min, 1 h, and 24 h assemblies are indistinguishable, suggesting that HT shell assembly is complete in under 2 min. (C). Representative TEM micrographs of shells assembled directly on carbon grids and stained immediately. These images show that many individual shells assemble within a short time period.

We sought to minimize the time between assembly and purification to mitigate potential adverse effects on biotic cargo due to prolonged urea exposure. We tested the completion of the assembly reaction after 2 min, 1 h, and 24 h. In all cases, only assembled shells elute from the size exclusion column (Figure 3B). Additionally, we performed an assembly reaction and immediately applied it on grids for negative stain TEM analysis, essentially capturing the state of the assembly reaction after 10 s (Figure 3C). TEM images showed many assembled shells, suggesting that individual shells assemble on time scales much faster than our ability to detect them with this method.

LOADING OF NON-NATIVE, CATALYTICALLY ACTIVE CARGO

Targeted Loading of the Enzyme NrfA via Shell Protein Conjugation. To demonstrate the application of *in vitro* BMC shell assembly for the encapsulation of catalytic cargo, we investigated the targeted loading of a non-native enzyme, cytochrome c nitrite reductase (NrfA) from *Geobacter lovleyi*.[31] Using the SpyTag–SpyCatcher system,[32,33] we covalently tethered cargo enzyme molecules to modified shell proteins. Specifically, we expressed and purified a construct of the BMC-T subunit with a SpyTag linker cloned to a loop region of the protein, previously shown to tolerate insertions.[20] The linker is located on the interior facet of the shell component in the assembled state. We investigated the ability of the BMC-T tile modified with SpyTag (referred to here onward as $_{\text{SpyT}}$BMC-T) to assemble into HT and HTP shells *in vitro* and found that they were successfully incorporated into assembled shells, though at a slightly lower efficiency than that of untagged BMC-T tiles (Figure S6). We also cloned, expressed, and purified NrfA with a SpyCatcher linker attached to the N-terminus (referred to here as NrfA$_{\text{SpyC}}$).

Because BMC-T tiles consist of three identical protomer subunits, the $_{\text{SpyT}}$BMC-T construct results in a tile that contains three SpyTags. Binding all three SpyTags with NrfA$_{\text{SpyC}}$ makes the protein considerably bulkier and less

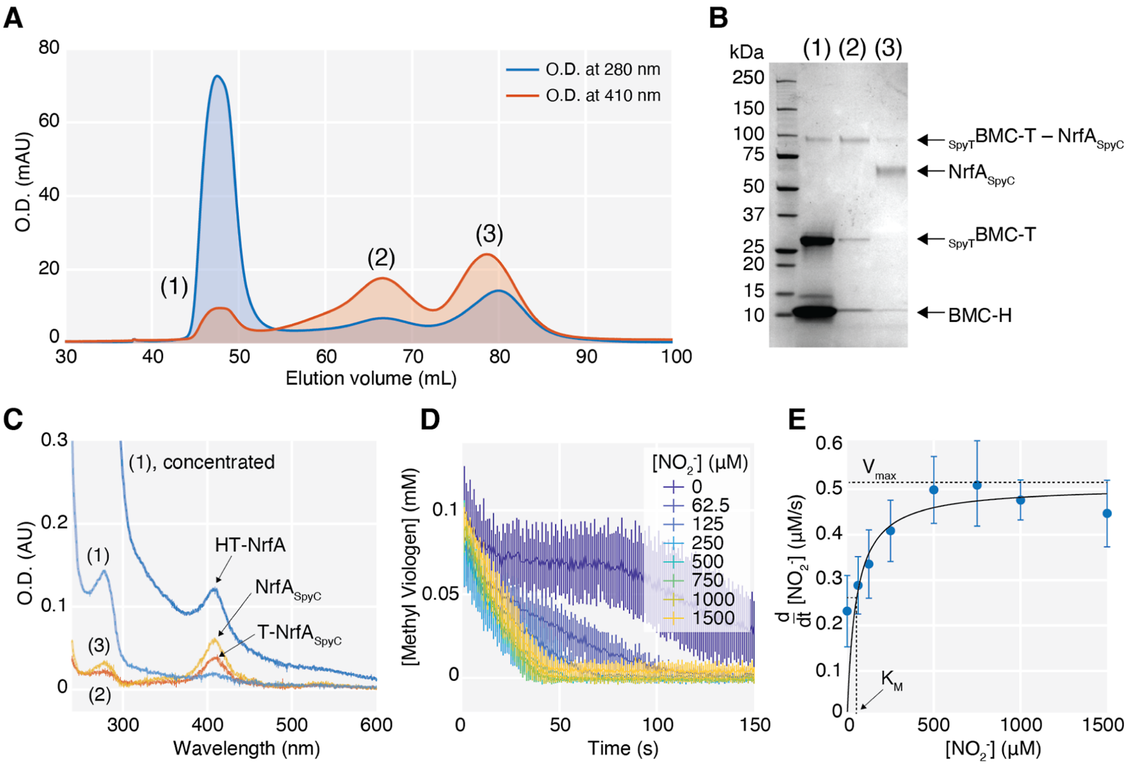

Figure 4. *In vitro* encapsulated NrfA$_{SpyC}$ is catalytically active. (A). SEC chromatogram showing purification of NrfA$_{SpyC}$-loaded HT wiffle shells from unincorporated BMC-H, $_{SpyT}$BMC-T, and NrfA$_{SpyC}$. (B). SDS-PAGE analysis shows the $_{SpyT}$BMC-T−NrfA$_{SpyC}$ conjugate in the elution peak (1) fraction containing HT shells and unincorporated conjugated $_{SpyT}$BMC-T−NrfA$_{SpyC}$ and unconjugated NrfA$_{SpyC}$ in peaks (2) and (3), respectively. (C). UV−vis spectra of SEC fractions for peaks (1−3) and a concentrated solution of (1). (D). Activity assay of NrfA$_{SpyC}$ inside HT shells in peak (1). Kinetic traces of the concentration of reduced methyl viologen at various concentrations of nitrite show the rates of substrate turnover. (E). Michaelis−Menten curve, with V_{max} = 0.502 ± 0.040 μM/s and K_M = 49.45 ± 25.47 μM.

viable for assembly. To prevent oversaturation of single $_{SpyT}$BMC-T tiles, we conjugated using an approximate ratio of 6 tiles per 1 enzyme or 3 enzymes per one shell. We conducted the conjugation reaction before assembly for 1 h on ice. Following incubation, we diluted the mixture of linked $_{SpyT}$BMC-T and NrfA$_{SpyC}$ in assembly buffer before the addition of BMC-H. We incubated the assembly reaction for 1 h on ice before loading the sample onto a size exclusion column. NrfA contains five internal c-type hemes absorbing at 410 nm in the Fe3+ oxidation state, allowing us to track the elution of the enzyme at a wavelength distinct from that of shell protein absorption (Figure 4A).

We observed conjugated $_{SpyT}$BMC-T−NrfA$_{SpyC}$ in the same fractions as those of assembled shells, as verified by SDS-PAGE (Figure 4B), and confirmed that conjugation of the enzyme to tile did not disrupt or change shell morphology by using DLS and TEM (Figure S7). Control SEC runs without the addition of BMC-H showed that the $_{SpyT}$BMC-T−NrfA$_{SpyC}$ conjugate as well as unconjugated $_{SpyT}$BMC-T and NrfA$_{SpyC}$ did not elute in the void volume (Figure S8A). Furthermore, wild-type NrfA is not encapsulated in the shells, indicating that nonspecific loading of the enzyme cargo does not occur in the absence of the SpyCatcher linkage (Figure S8B,C). The concentration of the enzyme inside the shells was measured via UV−vis absorbance of the heme Soret peak at 410 nm (Figures 4C and S9) and was found to be approximately 112 nM. Using the absorbance at 280 nm to extract an estimation for the concentration of HT shells, we calculated yields of roughly 425 nM shells, indicating an approximate loading efficiency of 26%, or roughly 1 enzyme per 4 HT shells. The large amount of NrfA$_{SpyC}$ that remains either unconjugated or unincorporated into the shells (peaks (3) and (2), respectively, in Figure 4A−C) suggests that the encapsulation efficiency can be improved by changing the reaction parameters, such as increasing the amount of cargo in the reaction. For example, we demonstrate that by lowering the overall subunit concentration and increasing the amount of NrfA$_{SpyC}$, we achieve an approximate loading efficiency of 1.5 enzymes per HT shell (Figure S10).

To evaluate the catalytic activity of the encapsulated enzyme, we performed a Michaelis−Menten enzyme activity assay on SEC-purified HT shells loaded with NrfA$_{SpyC}$ at a target concentration of 1 nM NrfA$_{SpyC}$ in the final reaction mixture. NrfA catalyzes the conversion of nitrite (NO_2^-) to ammonium, driven by electron donation from dithionite-reduced methyl viologen. To measure the rate of nitrite reduction by NrfA$_{SpyC}$, we monitored the change in absorbance as the solution containing reduced methyl viologen turns from blue to clear upon oxidation by the turnover of nitrite by NrfA$_{SpyC}$ (Figure 5D). The rates of reaction at early time points and at various substrate concentrations were fit to a hyperbolic Michaelis−Menten curve, from which K_M was measured to be 49.45 ± 25.47 μM, and V_{max} was 0.502 ± 0.040 μM/s (Figure 5E). The K_M is higher than that of the wild-type enzyme free in solution (27 ± 2 μM),[31] suggesting a decrease in accessibility of the substrate to the active site. This is potentially due to the barrier imposed by the HT shell. The rate of catalysis, k_{cat}, was inferred to be about 536 ± 68 μmol NO_2^- min^{-1} mg^{-1} enzyme. While this value of k_{cat} is lower than that of the wild-type enzyme (1291 ± 34 μmol NO_2^-

https://doi.org/10.1021/acsnano.4c15538
ACS Nano 2025, 19, 11913−11923

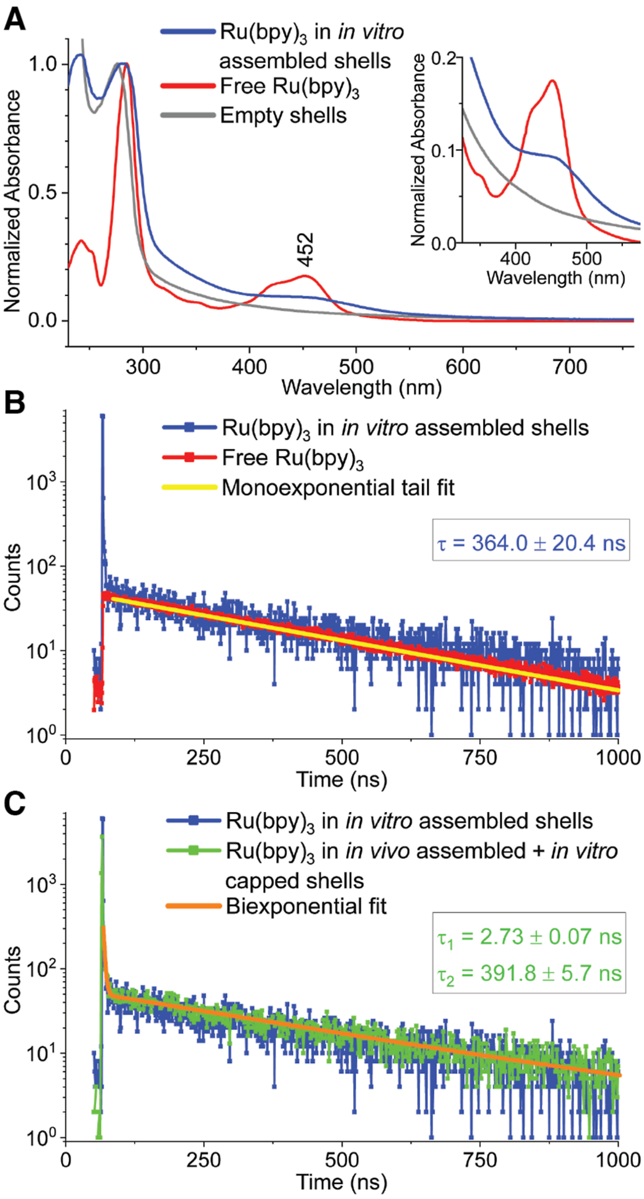

Figure 5. Spectroscopic data of the abiotic cargo molecule, Ru(bpy)$_3$, encapsulated in HTP shells by the one-step IVA method. (A). UV−vis spectra. Data are normalized by absorption at the bands around 277−285 nm in the UV region, and a magnification is shown for the region containing MLCT bands (inset). (B−C). TCSPC photoluminescence data are shown with indicated lifetimes derived from fitting with (B). monoexponential or (C). biexponential functions. Emission was measured at 620 nm using pulsed laser excitation at 445.8 nm.

min^{-1} mg^{-1} enzyme),[31] measurements of these parameters are in general sensitive to slight differences in experimental conditions, and additionally, our enzyme concentration determination has a large margin of error. Importantly, these data show that NrfA$_{\mathrm{SpyC}}$ inside HT shells remains catalytically active after conjugation and encapsulation.

Encapsulation of the Ru(bpy)$_3$ Photosensitizer via Passive Diffusion. To demonstrate an application of our in vitro BMC shell assembly for the encapsulation of a different non-native cargo, we investigated the loading of abiotic cargo molecules. A recent study showed that the abiotic molecule and benchmark photosensitizer, [Ru(bpy)$_3$]$^{2+}$, could be encapsulated via diffusion through the vacancies in *in vivo* assembled HT shells and then trapped in the shell lumen upon *in vitro* capping with the pentamer to form sealed HTP shells.[26] Our one-step IVA method outlined here was able to successfully encapsulate Ru(bpy)$_3$ at comparable cargo loading efficiencies to the former *in vivo* assembly + *in vitro* capping method (Table S3). Ru(bpy)$_3$Cl$_2$·6H$_2$O was dissolved in the shell protein solutions to a concentration of 13 mM immediately prior to initiation of shell assembly and subsequent separation of unassembled proteins and excess, unencapsulated Ru(bpy)$_3$ (see Methods). This IVA resulted in the cargo loading of ~20−22 Ru(bpy)$_3$ molecules per shell and required no specific interactions between shell proteins and abiotic cargo molecules for successful encapsulation. It should also be noted that these data indicate that the IVA method results in a significant population of sealed, complete shells because control studies have shown that Ru(bpy)$_3$ molecules will not remain in the shell lumen unless the shell is complete, i.e., without any vacancies from a missing shell protein.[26]

UV−vis characterization of the *in vitro* assembled shells harboring Ru(bpy)$_3$ showed a metal-to-ligand charge transfer (MLCT) band centered around 452 nm, as expected from the spectrum of free Ru(bpy)$_3$, although the shape of the band is somewhat skewed by scattering from the shell that raises the baseline (Figure 5A). The excited state lifetime was evaluated with time correlated single photon counting (TCSPC) photoluminescence spectroscopy. The spectrum of Ru(bpy)$_3$ encapsulated within the *in vitro* assembled shells has two time components, one of which is in agreement with that reported in the literature and measured here for free Ru(bpy)$_3$, with a lifetime of ~360 ns when tail-fitting the data with a monoexponential function (Figure 5B).[34,35] There is a much faster decaying species that is absent from the free Ru(bpy)$_3$ spectrum but overlays well with the spectrum of Ru(bpy)$_3$ in shells assembled by the former combined *in vivo* assembly + *in vitro* capping method with a determined lifetime of ~3 ns when fit with a biexponential function (Figure 5C). This faster decaying time component was attributed to possible intermolecular interactions of the Ru(bpy)$_3$ excited state with neighboring excited or ground state Ru(bpy)$_3$ molecules,[26] drawing upon a literature precedent for Ru(bpy)$_3$ in confinement in zeolites.[36] Collectively, the spectroscopic data for Ru(bpy)$_3$ encapsulated in shells via the IVA method mirror those of Ru(bpy)$_3$ loaded by the *in vivo* assembly + *in vitro* capping method, wherein the photosensitizers in that work were shown to retain their capabilities as visible light-driven electron donors.[26] While the two assembly methods result in comparable cargo loading efficiencies and nearly identical photophysics for Ru(bpy)$_3$, the IVA method is set apart by its speed and simplicity for benchtop assembly of shells around biotic or abiotic compounds using customizable protein building blocks to tune the microenvironment and optimize complex chemistries in confinement.

DISCUSSION

Our chaotropic IVA method provides several significant advancements in the production of BMC shells. Among the most notable of these improvements are the efficiency and speed of shell assembly. In contrast with the IVA method utilizing enzymatic cleavage,[23] our method approaches maximal efficiency; nearly all constituents in the reaction mixture are used to form monodisperse shells. By combining assembly competent BMC-H and BMC-T tiles, our method drastically reduces reaction incubation time to under 2 min. This increase in speed is likely an effect of the rapid mixing of assembly competent shell subunits, which are combined at concentrations that are higher than what are achievable via protease cleavage or *in vivo* expression methods. Furthermore, this method is able to generate highly pure shells through our ability to assemble shells using only their constituent protein building blocks. It diminishes the presence of contaminating cytosolic proteins or enzymatic cleavage products that are unavoidable in shells prepared by other *in vivo* protocols and the previously developed *in vitro* method. Shell assembly yields scale proportionally with increasing amounts of reaction components, highlighting the potential application of the technique in the large-scale production of BMC shells.

The assembly of shells is highly reproducible and robust across a wide range of urea concentrations (Figures S2 and S3). Interestingly, assemblies performed at higher urea concentrations exhibit lower polydispersity, as indicated by deeper oscillations in the SAXS spectra (Figure S2) and shown by the smaller number of polymorphisms observed by TEM (Figure S3). This suggests a possible avenue for controlling the shell size distribution and avoiding kinetic traps along the assembly pathway by modulating the chaotrope concentration. On the other hand, as a platform for encapsulating a wide variety of cargo, exposure to urea may also be minimized to avoid negative effects on sensitive biotic cargo such as enzymes. Previous studies that explored the denaturing effects of urea on proteins have typically observed significant protein denaturation at concentrations in the range of 6−8 M.[37,38] Our urea-based assemblies are typically performed at concentrations lower than 500 mM, leading to less severe destabilizing effects. Sensitivity to urea can vary significantly, and thus, biotic cargo stability must be screened prior to encapsulation using chaotropic shell assembly.

This method for the synthesis of BMC shells provides additional enhanced versatility through the ability to control the order of addition for cargo loading of HTP shells. This offers advantages over the combined *in vivo* assembly + *in vitro* capping protocol, such as the potential to encapsulate bulkier enzymatic cargo or abiotic compounds, like nanoparticles, that are too large to fit through the vacancies in HT wiffle shells. In these cases, assembly of complete shells around larger cargo can be approached via nonspecific encapsulation or through targeted linkages. Nonspecific encapsulation minimizes reaction steps but reduces control over assembly and requires higher cargo concentrations to increase loading efficiency. A targeted approach, such as the SpyTag−SpyCatcher system, provides increased control over assembly at much lower cargo concentrations. However, a potential limitation with this approach is the binding of multiple cargo entities to a single tile, creating bulkiness that may obstruct assembly. This can likely be mitigated by varying the ratio of cargo and tiles to prevent oversaturation. In the case of NrfA, it is a multiheme enzyme that matures and functions in the periplasm. As such, coexpression with shell proteins is not a suitable method of generating encapsulated NrfA in BMC shells *in vivo*; therefore, from the initially modest encapsulation of 26% of functionally active enzymes to an increased encapsulation of 1.5 NrfA enzymes per shell, both illustrate significant new-to-nature compartmentalization.

As a powerful tool for bioengineering efforts, our method allows the substitution of native tiles with modified tiles, enabling the assembly of shells with alternate functionality and properties such as cargo binding affinity and permeability. Peptide extensions known as encapsulation peptides (EPs) are used to pack BMC shells with native enzymes.[39−42] However, loading shells using EPs is typically inefficient,[17,19,43] and the precise nature of the binding of EPs to shells is not well-defined across shell systems. Our method overcomes this shortcoming by using modified tiles, such as $_{\mathrm{SpyT}}$BMC-T, thus providing an avenue for covalent cargo encapsulation. *In vivo* encapsulation by targeted loading using affinity tags is time- and labor-intensive as testing maximum cargo loading can only be done through varying inducer concentrations.[44] Our *in vitro* method offers more precise control over tile/cargo ratios and allows quicker screening and optimization for shell assembly. Studies have shown that the central pores of the shell tiles determine the permeability of shells to metabolites.[45−47] Therefore, shell tiles can be designed with mutations that alter overall shell permeability,[48−50] increasing control of flux of diffusible metabolites.[51] Control over all of the aforementioned parameters and properties by using modified tiles interchangeably increases loading capability and capacity for any specific catalytically relevant cargo.

CONCLUSIONS

Our work presents a new, efficient, and fast method for IVA of BMC shells that can be used in a variety of applications, such as construction of highly specific nanoreactors. This chaotrope-based approach overcomes the barrier to the *in vitro* synthesis of shells presented by insoluble BMC-H sheets, which are not viable for shell assembly. The necessary amount of urea needed to disrupt BMC-H sheet structures has proven to be optimal for remarkably robust assembly, allowing increased control and efficiency through the simplicity of combining the three general constituents for shell assembly without additional enzymatic steps. Demonstrated through our ability to incorporate a modified shell tile, our method broadens the scope for bioengineered shells that can be designed for specific applications. The successful encapsulation of biotic and abiotic cargo, both resulting in new-to-nature compartmentalized catalysis, provides evidence of the significant advantage of our method over *in vivo* synthesis and the former *in vitro* shell assembly method.

METHODS

Expression and Purification of BMC Shell Proteins. BL21-(DE3) chemically competent cells (New England Biolabs) were transformed with plasmid DNA containing BMC shell protein sequences according to the vendor's specifications. Cells were incubated with 50−100 ng of plasmid DNA on ice for 30 min and heat shocked at 42 °C for 10 s. Cells were then placed back on ice for 5 min before adding 950 μL of Luria−Bertani broth for 1 h at 37 °C with gentle shaking. 100 μL of recovered cells was plated on kanamycin or ampicillin plates depending on the selective marker in each plasmid, and colonies were grown overnight at 37 °C.

Colonies of transformed BL21(DE3) cells were grown in 50 mL of Luria−Bertani broth at 37 °C overnight. They were grown with 100 μg/mL ampicillin or 50 μg/mL kanamycin, depending on the selective marker in the plasmid. Cells were induced at OD 0.6−0.8 at 600 nm with 50 μL of 1 mg/mL anhydrotetracycline (aTc) (for BMC-T, $_{\mathrm{SpyT}}$BMC-T, and BMC-P expressions) or 500 μL of 1 M IPTG (for BMC-H expression) per 1 L of culture. The induced cells were incubated at 22 °C for 18 h. The cells were pelleted by centrifugation at 8000 rpm for 20 min at 4 °C with a JLA 8.1 rotor in a Beckman Coulter Avanti J-26 XP centrifuge, and the supernatant was discarded. Cell pellets were stored at −20 °C.

Purification of BMC-T, $_{\text{SpyT}}$BMC-T, and BMC-P Using Affinity Chromatography. Frozen cell pellets were thawed on ice and resuspended in 30 mL of Lysis Buffer (50 mM Tris pH 8, 300 mM NaCl, 10 mM imidazole, 5% v/v glycerol) with the addition of 1/2 Sigma protease inhibitor tablet and 200 μL of 2 mg/mL DNase I. Cells were lysed by passage through an Avestin Emulsiflex C3 Homogenizer at 20,000 psi three times. Cell lysate was clarified by centrifugation at 20,000 rpm for 1 h at 4 °C with a JA 20 rotor in a Beckman Coulter Avanti J-26 XP centrifuge. Supernatants were filtered using a 0.22 μm filter and transferred to clean tubes. Column chromatography was performed using an ÄKTA Start chromatography system (GE Healthcare), and clarified lysates were applied to a 5 mL HisTrap column (GE Healthcare) that was equilibrated with Buffer A (20 mM Tris−HCl pH 8, 500 mM NaCl). The column was washed with 6 CV of Buffer A and then subsequently washed with 6 CV of 98% Buffer A and 2% Buffer B (20 mM Tris−HCl pH 8, 500 mM NaCl, 500 mM Imidazole). Protein was eluted over a ten-column volume gradient from 4−100% Buffer B. Fractions containing the target protein were identified by SDS-PAGE analysis and were pooled and concentrated with a 3 kDa MWCO Amicon Ultra centrifugal filter (EMD Millipore). Using an ÄKTA Pure protein purification system, proteins were loaded onto Superdex 200 Increase 10/300 GL by Cytiva. Proteins were eluted in SEC Buffer (50 mM Tris−HCl pH 8, 150 mM NaCl) using a flow rate of 0.5 mL/min. Protein concentrations were quantified by measuring the A280 with a NanoDrop UV−vis (Thermo) and using the theoretical extinction coefficients (Table S2).

Purification of BMC-H Sheet Inclusion Bodies. The protocol for purifying BMC-H sheets from inclusion bodies was adopted and slightly modified from Sutter et al.[24] Frozen cell pellets from 1 L culture were resuspended in 30 mL of Hexamer Lysis Buffer (50 mM Tris−HCl pH 8, 100 mM NaCl, 10 mM $MgCl_2$), 200 μL of 2 mg/mL DNase 1, and 100 μL of 10 mg/mL lysozyme. Cells were lysed by 3 passes through an Avestin Emulsiflex C3 Homogenizer at 20,000 psi. 300 μL of Triton X-100 (1% v/v) was added to the lysate and incubated at room temperature with gentle agitation for 20 min on an orbital shaker. Insoluble material was separated by centrifugation for 20 min at 20,000 rpm with a JA 20 rotor in a Beckman Coulter Avanti J-26 XP centrifuge. The supernatant was discarded, and the white pellet was resuspended in 30 mL of Hexamer Wash Buffer (50 mM Tris−HCl pH 8, 100 mM NaCl, 10 mM $MgCl_2$, 1% v/v Triton X-100) without disturbing the brown cellular debris. The resuspension was transferred to a new centrifuge tube. The centrifugation/wash steps were repeated with 20−30 mL of Hexamer Wash Buffer until the pellet was visibly more white and cellular debris was absent. The pellet was then washed once with 30 mL of Hexamer Lysis Buffer to remove Triton X-100. The pellet was then resuspended in 10 mL of Hexamer Lysis Buffer and stored at 4 °C.

BMC-H Sheet Denaturation. In an Eppendorf tube, approximately 10−15 mg of BMC-H sheets was spun in a centrifuge at 13,500 rcf for 10 min. After the supernatant was decanted, the pellet was resuspended in Tris buffer (10 mM) with 500 mM urea. The resuspension was incubated at 25 °C overnight on an orbital shaker with gentle shaking before repeating centrifugation at 13,500 rcf for 10 min. The supernatant was transferred to a separate tube without disturbing the remaining pellet. Protein concentration was quantified by measuring the A280 with a NanoDrop UV−vis (Thermo) and using the theoretical extinction coefficient (Table S2). Solubilized BMC-H tiles were stored at 4 °C.

Cloning, Expression, and Purification of Cytochrome c NrfA$_{\text{SpyC}}$. NrfA$_{\text{SpyC}}$ was cloned from an existing vector[35] containing a codon-optimized sequence for NrfA from G. lovleyi, an N-terminal pelB periplasmic localization signal, and a C-terminal Strep-tag II on a pBAD202/D-TOPO backbone. The pBAD backbone was PCR amplified with primers containing sequence overlaps with SpyC. SpyC was PCR amplified with primers that overlapped the pelB region and NrfA. SpyC was inserted by Gibson assembly using the Gibson Assembly Master Mix from New England Biolabs. After mixing PCR products and the master mix, samples were incubated for 15 min at 50 °C. Gibson assembled products were transformed into BL21*E. coli* and selected for kanamycin resistance. Resistant colonies were picked, and plasmid DNA was isolated using a New England Biolabs Plasmid DNA Miniprep Kit. Assembly junction sites were then sequenced by Sanger sequencing at the Michigan State University Genomics Core.

NrfA$_{\text{SpyC}}$ was expressed in*Shewanella oneidensis* transformed with a pBAD vector containing NrfA with a pelB periplasmic localization sequence, N-terminal SpyCatcher001 and a C-terminal Strep-tag II. Cultures were grown in TB media at 30 °C while being shaken at 160 rpm. Cultures were then induced with a final concentration of 0.02% arabinose at an OD600 between 0.6 and 0.7 followed by a 16 h expression at 30 °C and 160 rpm and subjected to osmotic shock to lyse the periplasmic space. To perform osmotic shock, cell cultures were pelleted and resuspended in a 20% sucrose solution containing 1 mM EDTA and 30 mM Tris-base at pH 8.0. Cells were then pelleted again and resuspended in ice cold Milli-Q water. The resuspension in ice water was pelleted, and the supernatant (lysate) was collected and buffered with Wash Buffer (100 mM Tris−HCl, 150 mM NaCl, 0.1 mM EDTA) with the addition of one complete-mini EDTA-free protease inhibitor tablet from Sigma-Aldrich per liter of culture. The lysate was then filtered and purified with affinity purification on a Strep-Tactin XT 4 flow column from IBA Lifesciences and eluted with 50 mM biotin in Wash Buffer at pH 8.0. To further remove contaminants, the eluted protein solution was concentrated on a 10 kDa MWCO centrifugal filter unit from Sigma-Aldrich and subjected to SEC on a Superdex 200 Increase 10/300 GL column from Cytiva. All chromatography steps were performed on a Biorad NGC chromatography system. Samples were flash frozen with liquid nitrogen and stored at −80 °C.

***In Vitro* Assembly.** To assemble HT and HTP shells, we added BMC-T (and BMC-P) to IVA buffer (50 mM Tris−HCl at pH 8.0, 150 mM NaCl, 10% v/v glycerol) on ice, mixing thoroughly before adding BMC-H and mixing thoroughly again. The amount of shell proteins added to the reactions was determined by calculating the desired final concentrations of shell proteins. The final concentrations of urea in the assembly reactions varied from 80 mM to 200 mM, depending on the initial concentrations of BMC-H used in the assembly. For many of the assemblies reported in the main text, the final concentrations of BMC shell protein tiles were 1 mg/mL BMC-H (16.5 μM tile), 0.33 mg/mL BMC-T (4.8 μM trimer tile), and 1 mg/mL BMC-P (18.3 μM pentamer tile). The assembly reactions were typically incubated for 1 h to overnight at 4 °C.

SEC Purification of Assembled Shells. An ÄKTA Pure protein purification system was used, and samples were loaded onto either the Superdex 200 Increase 10/300 GL by Cytiva or the HiLoad 16/600 Superdex 200 pg by Sigma-Aldrich depending upon sample volume. Samples were eluted in SEC Buffer using a flow rate of 0.5 mL/min for the Superdex 200 increase 10/300 or 1 mL/min for the HiLoad 16/600 Superdex pg.

Dynamic Light Scattering. Experiments were performed on a Zetasizer Nano S instrument (Malvern). Measurements were taken with 10 acquisitions for 10 s each at room temperature using the particle sizing Standard Operating Procedure with default parameters.

TEM Analysis. Ten μL of shell samples was incubated on glow-discharged 300 mesh Formvar-coated TEM grids (Ted Pella) for 1 min, wicked off with Whatman filter paper, washed 3 times in droplets of water, and stained with 10 μL of 1% uranyl acetate for 1 min. Excess uranyl acetate was wicked off with a Whatman filter paper. Grids were left to air-dry and imaged using a Tecnai-12 transmission electron microscope (FEI) operated at 120 kV. Images were recorded on a Gatan 2K *x* 2K-pixel CCD camera.

Small-Angle X-ray Scattering. SAXS measurements were performed at two beamlines: 12-ID-B of the advanced photon source (APS) at Argonne National Laboratory and LiX Beamline 16-ID of NSLS2 at Brookhaven National Laboratory. The X-ray energy of the APS 12-ID-B beamline was 13.3 keV, and the SAXS data were collected using an Eiger2S 9 M detector (Dectris Ltd.). For the LiX beamline, the X-ray energy was 15 keV, and measurements were performed using a Pilatus3 1 M detector (Dectris Ltd.). In both cases, flow cells were employed to minimize the potential radiation damage.

NrfA Cargo Loading and Methyl Viologen Activity Assay. To encapsulate $\mathrm{NrfA_{SpyC}}$ inside HT shells, we mixed the enzyme with $_{\mathrm{SpyT}}$BMC-T such that the final ratio of enzymes to assembled shells was approximately 3 enzymes per complete shell, assuming 100% assembly efficiency. The $_{\mathrm{SpyT}}$BMC-T + $\mathrm{NrfA_{SpyC}}$ mixture was incubated on ice for 1 h before addition of BMC-H. The assembly reaction mixture was incubated on ice for 1 h before loading onto a HiLoad 16/600 Superdex 200 pg size exclusion column. The eluted fractions containing assembled NrfA-loaded HT shells were collected and concentrated at 14,000 rcf in a 100 kDa Amicon Ultra centrifugal filter. The presence of NrfA in these fractions was confirmed using UV−vis spectroscopy, and the concentration was quantified by fitting the heme absorbance peak at 410 nm (Figure S8).

We tested the activity of the NrfA inside HT shells using a Michaelis−Menten enzyme activity assay adapted from Campecino et al.[31] with modifications. We added the SEC-purified NrfA-loaded HT shells to NrfA Activity Buffer (50 mM Tris−HCl pH 8, 150 mM NaCl, 0.8 mM methyl viologen, and 0.1 mM sodium dithionite) to a target enzyme concentration of 1 nM. This solution is a deep blue color due to the presence of dithionite-reduced methyl viologen. In a 96-well clear-bottom plate mounted on a white light source, we added 190 μL of the enzyme solution to 10 μL of various concentrations of nitrite. Using an Arducam USB-powered RGB camera mounted directly above the plate, we took videos of the wells in the plate at a rate of 1 frame per second. We monitored the progression of the enzyme reaction over time as the solutions in the wells turned from blue to clear. Using MATLAB software, triplicate readings of the kinetic traces were extracted by integrating the pixel intensities within each image's blue channel corresponding to each well, and the pixel intensities were correlated to the initial reduced methyl viologen concentration of 0.1 mM, as measured by the NanoDrop UV−vis. The rate of change in methyl viologen concentration was found by fitting the first 10 s of replicate absorbance readings to a line. The enzyme reaction rates were then fitted to a hyperbolic curve using the curve_fit function from the scipy.optimize Python package to obtain the Michaelis−Menten parameters.

Ru(bpy)3 Cargo Loading and TCSPC Photoluminescence Spectroscopy. The IVA was performed as outlined above, with the exception that solid $\mathrm{Ru(bpy)_3Cl_2{\cdot}6H_2O}$ (Sigma-Aldrich) was dissolved in each of the shell protein solutions to a concentration of ∼13 mM immediately prior to initiating assembly with the addition of BMC-H to the solution of BMC-T and BMC-P. The assembly reaction took place for one h at room temperature before loading the sample on the top of a sucrose cushion (20 mM Tris, pH 7.4, 50 mM NaCl, 30% w/v sucrose) followed by centrifugation overnight at ∼200,000 rcf and 4 °C. The next day, the supernatant was discarded, and the pellet was resuspended in HBS (20 mM HEPES, pH 7.4, 50 mM NaCl). The sample was then concentrated and resuspended four times in HBS using 0.5 mL of 100 kDa MWCO Amicon Ultra centrifugal filters to filter out trace remaining unencapsulated $\mathrm{Ru(bpy)_3}$. Protein and ruthenium concentrations were then determined by Bradford assay and inductively coupled plasma atomic emission spectroscopy, respectively.

TCSPC photoluminescence spectra were measured on a FLS 1000 photoluminescence spectrometer (Edinburgh Instruments) with a PMT-980 detector. An EPL-450 ps pulsed diode laser with a 1 s pulse period was used for excitation at 445.8 nm, and emission was measured at 620 nm using a 455 nm long pass filter to remove reflected and elastically scattered light from the signal. Decay spectra were fit with either a monoexponential function using Fluoracle software or a biexponential function using OriginLab 2022 software. All samples were measured in 20 mM HEPES, pH 7.4, and 50 mM NaCl.

ASSOCIATED CONTENT

Supporting Information

The Supporting Information is available free of charge at https://pubs.acs.org/doi/10.1021/acsnano.4c15538.

Additional protein details; analysis of size and monodispersity of shells and shell proteins; comparative method analysis for Ru(bpy)3 loaded shells; analysis of shell size distributions at different urea concentrations; additional experimental results addressing assembly speed, efficiency, and reproducibility; cargo loading assembly controls; quantification of cargo in loaded shells; and enhanced cargo encapsulation (PDF)

AUTHOR INFORMATION

Corresponding Authors

Markus Sutter − *MSU-DOE Plant Research Laboratory, Michigan State University, East Lansing, Michigan 48824, United States; Environmental Genomics and Systems Biology Division, Lawrence Berkeley National Laboratory, Berkeley, California 94720, United States; Molecular Biophysics and Integrated Bioimaging Division, Lawrence Berkeley National Laboratory, Berkeley, California 4720, United States;* orcid.org/0000-0001-6290-4820; Email: msutter@lbl.gov

Cheryl A. Kerfeld − *MSU-DOE Plant Research Laboratory, Michigan State University, East Lansing, Michigan 48824, United States; Environmental Genomics and Systems Biology Division, Lawrence Berkeley National Laboratory, Berkeley, California 94720, United States; Molecular Biophysics and Integrated Bioimaging Division, Lawrence Berkeley National Laboratory, Berkeley, California 4720, United States; Department of Biochemistry and Molecular Biology, Michigan State University, East Lansing, Michigan 48824, United States;* orcid.org/0000-0002-9977-8482; Email: ckerfeld@lbl.gov

Authors

Kyleigh L. Range − *MSU-DOE Plant Research Laboratory, Michigan State University, East Lansing, Michigan 48824, United States; Molecular Foundry Division, Lawrence Berkeley National Laboratory, Berkeley, California 94720, United States;* orcid.org/0009-0009-4333-7539

Timothy K. Chiang − *Molecular Foundry Division, Lawrence Berkeley National Laboratory, Berkeley, California 94720, United States;* orcid.org/0009-0000-5811-9221

Arinita Pramanik − *Molecular Foundry Division, Lawrence Berkeley National Laboratory, Berkeley, California 94720, United States*

Joel F. Landa − *Cell and Molecular Biology Department and Molecular Plant Sciences Program, Michigan State University, East Lansing, Michigan 48824, United States;* orcid.org/0000-0003-1882-6698

Samuel N. Snyder − *Chemical Sciences and Engineering Division, Argonne National Laboratory, Lemont, Illinois 60439, United States;* orcid.org/0000-0002-2571-4048

Xiaobing Zuo − *X-ray Science Division, Argonne National Laboratory, Lemont, Illinois 60439, United States*

David M. Tiede − *Chemical Sciences and Engineering Division, Argonne National Laboratory, Lemont, Illinois 60439, United States;* orcid.org/0000-0002-2784-4954

Lisa M. Utschig − *Chemical Sciences and Engineering Division, Argonne National Laboratory, Lemont, Illinois 60439, United States;* orcid.org/0000-0003-2095-5392

Eric L. Hegg − *Cell and Molecular Biology Department, Molecular Plant Sciences Program, and Department of Biochemistry and Molecular Biology, Michigan State*

University, East Lansing, Michigan 48824, United States; orcid.org/0000-0003-2055-5495

Corie Y. Ralston − *Molecular Foundry Division, Lawrence Berkeley National Laboratory, Berkeley, California 94720, United States; Molecular Biophysics and Integrated Bioimaging Division, Lawrence Berkeley National Laboratory, Berkeley, California 4720, United States;* orcid.org/0000-0002-7899-0951

Complete contact information is available at: https://pubs.acs.org/10.1021/acsnano.4c15538

Author Contributions

◆K.L.R. and T.K.C. contributed equally to this work.

Notes

The authors declare no competing financial interest.
A preprint of this work is published in ref.52.

ACKNOWLEDGMENTS

We thank Dr. Andrew Hagen for designing the $_{\text{SpyT}}$BMC-T construct used in this study. We also thank Dr. Behzad Rad at the Molecular Foundry for assistance with troubleshooting instrumentation operation and sample preparation. This work was supported as part of the Center for Catalysis in Biomimetic Confinement, an Energy Frontier Research Center funded by the U.S. Department of Energy, Office of Science, Basic Energy Sciences under Award Number DE-SC0023395. The Molecular Foundry at Lawrence Berkeley National Laboratory is supported by the Director, Office of Science, Office of Basic Energy Sciences, US DOE under Contract DE-AC02-05CH11231. This research used resources of the Advanced Photon Source, a U.S. Department of Energy (DOE) Office of Science user facility at Argonne National Laboratory and is based on research supported by the U.S. DOE Office of Science-Basic Energy Sciences, under Contract No. DE-AC02-06CH11357. The LiX beamline is part of the Center for BioMolecular Structure (CBMS), which is primarily supported by the National Institutes of Health, National Institute of General Medical Sciences (NIGMS) through a P30 Grant (P30GM133893) and by the DOE Office of Biological and Environmental Research (KP1605010). LiX also received additional support from NIH Grant S10 OD012331. As part of NSLS-II, a national user facility at Brookhaven National Laboratory, work performed at the CBMS is supported in part by the U.S. Department of Energy, Office of Science, Office of Basic Energy Sciences Program under contract number DE-SC0012704.

REFERENCES

(1) Sutter, M.; Melnicki, M. R.; Schulz, F.; Woyke, T.; Kerfeld, C. A. A Catalog of the Diversity and Ubiquity of Bacterial Microcompartments. *Nat. Commun.* **2021**, *12* (1), 3809.

(2) Ochoa, J. M.; Yeates, T. O. Recent Structural Insights into Bacterial Microcompartment Shells. *Curr. Opin. Microbiol.* **2021**, *62*, 51−60.

(3) Kerfeld, C. A.; Aussignargues, C.; Zarzycki, J.; Cai, F.; Sutter, M. Bacterial Microcompartments. *Nat. Rev. Microbiol.* **2018**, *16* (5), 277−290.

(4) Huffine, C. A.; Zhao, R.; Tang, Y. J.; Cameron, J. C. Role of Carboxysomes in Cyanobacterial CO 2 Assimilation: CO 2 Concentrating Mechanisms and Metabolon Implications. *Environ. Microbiol.* **2023**, *25* (2), 219−228.

(5) Rae, B. D.; Long, B. M.; Badger, M. R.; Price, G. D. Functions, Compositions, and Evolution of the Two Types of Carboxysomes: Polyhedral Microcompartments That Facilitate CO 2 Fixation in Cyanobacteria and Some Proteobacteria. *Microbiol. Mol. Biol. Rev.* **2013**, *77* (3), 357−379.

(6) Kennedy, N. W.; Mills, C. E.; Nichols, T. M.; Abrahamson, C. H.; Tullman-Ercek, D. Bacterial Microcompartments: Tiny Organelles with Big Potential. *Curr. Opin. Microbiol.* **2021**, *63*, 36−42.

(7) Yeates, T. O.; Crowley, C. S.; Tanaka, S. Bacterial Microcompartment Organelles: Protein Shell Structure and Evolution. *Annu. Rev. Biophys.* **2010**, *39* (1), 185−205.

(8) Parsons, J. B.; Dinesh, S. D.; Deery, E.; Leech, H. K.; Brindley, A. A.; Heldt, D.; Frank, S.; Smales, C. M.; Lünsdorf, H.; Rambach, A.; Gass, M. H.; Bleloch, A.; McClean, K. J.; Munro, A. W.; Rigby, S. E. J.; Warren, M. J.; Prentice, M. B. Biochemical and Structural Insights into Bacterial Organelle Form and Biogenesis. *J. Biol. Chem.* **2008**, *283* (21), 14366−14375.

(9) Roberts, E. W.; Cai, F.; Kerfeld, C. A.; Cannon, G. C.; Heinhorst, S. Isolation and Characterization of the Prochlorococcus Carboxysome Reveal the Presence of the Novel Shell Protein CsoS1D. *J. Bacteriol.* **2012**, *194* (4), 787−795.

(10) Faulkner, M.; Rodriguez-Ramos, J.; Dykes, G. F.; Owen, S. V.; Casella, S.; Simpson, D. M.; Beynon, R. J.; Liu, L.-N. Direct Characterization of the Native Structure and Mechanics of Cyanobacterial Carboxysomes. *Nanoscale* **2017**, *9* (30), 10662−10673.

(11) Yang, M.; Simpson, D. M.; Wenner, N.; Brownridge, P.; Harman, V. M.; Hinton, J. C. D.; Beynon, R. J.; Liu, L.-N. Decoding the Stoichiometric Composition and Organisation of Bacterial Metabolosomes. *Nat. Commun.* **2020**, *11* (1), 1976.

(12) Trettel, D. S.; Resager, W.; Ueberheide, B. M.; Jenkins, C. C.; Winkler, W. C. Chemical Probing Provides Insight into the Native Assembly State of a Bacterial Microcompartment. *Structure* **2022**, *30* (4), 537−550.

(13) Parsons, J. B.; Frank, S.; Bhella, D.; Liang, M.; Prentice, M. B.; Mulvihill, D. P.; Warren, M. J. Synthesis of Empty Bacterial Microcompartments, Directed Organelle Protein Incorporation, and Evidence of Filament-Associated Organelle Movement. *Mol. Cell* **2010**, *38* (2), 305−315.

(14) Sutter, M.; McGuire, S.; Ferlez, B.; Kerfeld, C. A. Structural Characterization of a Synthetic Tandem-Domain Bacterial Microcompartment Shell Protein Capable of Forming Icosahedral Shell Assemblies. *ACS Synth. Biol.* **2019**, *8* (4), 668−674.

(15) Choudhary, S.; Quin, M. B.; Sanders, M. A.; Johnson, E. T.; Schmidt-Dannert, C. Engineered Protein Nano-Compartments for Targeted Enzyme Localization. *PLoS One* **2012**, *7* (3), No. e33342.

(16) Ferlez, B. H.; Kirst, H.; Greber, B. J.; Nogales, E.; Sutter, M.; Kerfeld, C. A. Heterologous Assembly of Pleomorphic Bacterial Microcompartment Shell Architectures Spanning the Nano- to Microscale. *Adv. Mater.* **2023**, *35* (23), 2212065.

(17) Cai, F.; Bernstein, S. L.; Wilson, S. C.; Kerfeld, C. A. Production and Characterization of Synthetic Carboxysome. Shells with Incorporated Luminal Proteins1. *Plant Physiol.* **2016**, *170*, 1868−1877.

(18) Ni, T.; Jiang, Q.; Ng, P. C.; Shen, J.; Dou, H.; Zhu, Y.; Radecke, J.; Dykes, G. F.; Huang, F.; Liu, L.-N.; Zhang, P. Intrinsically Disordered CsoS2 Acts as a General Molecular Thread for α-Carboxysome Shell Assembly. *Nat. Commun.* **2023**, *14* (1), 5512.

(19) Lassila, J. K.; Bernstein, S. L.; Kinney, J. N.; Axen, S. D.; Kerfeld, C. A. Assembly of Robust Bacterial Microcompartment Shells Using Building Blocks from an Organelle of Unknown Function. *J. Mol. Biol.* **2014**, *426* (11), 2217−2228.

(20) Hagen, A.; Sutter, M.; Sloan, N.; Kerfeld, C. A. Programmed Loading and Rapid Purification of Engineered Bacterial Microcompartment Shells. *Nat. Commun.* **2018**, *9* (1), 2881.

(21) Sutter, M.; Greber, B.; Aussignargues, C.; Kerfeld, C. A. Assembly Principles and Structure of a 6.5-MDa Bacterial Microcompartment Shell. *Science* **2017**, *356* (6344), 1293−1297.

(22) Greber, B. J.; Sutter, M.; Kerfeld, C. A. The Plasticity of Molecular Interactions Governs Bacterial Microcompartment Shell Assembly. *Structure* **2019**, *27* (5), 749−763.

(23) Hagen, A. R.; Plegaria, J. S.; Sloan, N.; Ferlez, B.; Aussignargues, C.; Burton, R.; Kerfeld, C. A. In Vitro Assembly of Diverse Bacterial Microcompartment Shell Architectures. *Nano Lett.* **2018**, *18* (11), 7030−7037.

(24) Sutter, M.; Faulkner, M.; Aussignargues, C.; Paasch, B. C.; Barrett, S.; Kerfeld, C. A.; Liu, L.-N. Visualization of Bacterial Microcompartment Facet Assembly Using High-Speed Atomic Force Microscopy. *Nano Lett.* **2016**, *16* (3), 1590−1595.

(25) Faulkner, M.; Zhao, L.-S.; Barrett, S.; Liu, L.-N. Self-Assembly Stability and Variability of Bacterial Microcompartment Shell Proteins in Response to the Environmental Change. *Nanoscale Res. Lett.* **2019**, *14* (1), 54.

(26) Snyder, S. N.; Jussupow, A.; Feig, M.; Potocny, A. M.; Sutter, M.; Kerfeld, C. A.; Mulfort, K. L.; Utschig, L. M. In Vitro Encapsulation of Functionally Active Abiotic Photosensitizers Inside a Bacterial Microcompartment Shell. *J. Phys. Chem. Lett.* **2024**, *15* (31), 8000−8006.

(27) Ferlez, B.; Sutter, M.; Kerfeld, C. A. A Designed Bacterial Microcompartment Shell with Tunable Composition and Precision Cargo Loading. *Metab. Eng.* **2019**, *54*, 286−291.

(28) Luque, A.; Reguera, D. The Structure of Elongated Viral Capsids. *Biophys. J.* **2010**, *98* (12), 2993−3003.

(29) Sutter, M.; Laughlin, T. G.; Sloan, N. B.; Serwas, D.; Davies, K. M.; Kerfeld, C. A. Structure of a Synthetic β -Carboxysome Shell. *Plant Physiol.* **2019**, *181* (3), 1050−1058.

(30) Cesle, E. E.; Filimonenko, A.; Tars, K.; Kalnins, G. Variety of Size and Form of GRM2 Bacterial Microcompartment Particles. *Protein Sci.* **2021**, *30* (5), 1035−1043.

(31) Campeciño, J.; Lagishetty, S.; Wawrzak, Z.; Sosa Alfaro, V.; Lehnert, N.; Reguera, G.; Hu, J.; Hegg, E. L. Cytochrome c Nitrite Reductase from the Bacterium Geobacter Lovleyi Represents a New NrfA Subclass. *J. Biol. Chem.* **2020**, *295* (33), 11455−11465.

(32) Zakeri, B.; Fierer, J. O.; Celik, E.; Chittock, E. C.; Schwarz-Linek, U.; Moy, V. T.; Howarth, M. Peptide Tag Forming a Rapid Covalent Bond to a Protein, through Engineering a Bacterial Adhesin. *Proc. Natl. Acad. Sci. U.S.A.* **2012**, *109* (12), E690−E697.

(33) Hatlem, D.; Trunk, T.; Linke, D.; Leo, J. C. Catching a SPY: Using the SpyCatcher-SpyTag and Related Systems for Labeling and Localizing Bacterial Proteins. *Int J Mol Sci* **2019**, *20* (9), 2129.

(34) Kalyanasundaram, K. Photophysics Photochemistry and Solar Energy Conversion with Tris(Bipyridyl)Ruthenium(II) and Its Analogues. *Coord. Chem. Rev.* **1982**, *46*, 159−244.

(35) Sciuto, E. L.; Santangelo, M. F.; Villaggio, G.; Sinatra, F.; Bongiorno, C.; Nicotra, G.; Libertino, S. Photo-Physical Characterization of Fluorophore Ru(Bpy)32+ for Optical Biosensing Applications. *Sens. BioSensing Res* **2015**, *6*, 67−71.

(36) Sykora, M.; Kincaid, J. R.; Dutta, P. K.; Castagnola, N. B. On the Nature and Extent of Intermolecular Interactions between Entrapped Complexes of Ru(Bpy)32+ in Zeolite Y. *J. Phys. Chem. B* **1999**, *103* (2), 309−320.

(37) Rajagopalan, K. V.; Fridovich, I.; Handler, P. Competitive Inhibition of Enzyme Activity by Urea. *J. Biol. Chem.* **1961**, *236*, 1059−1065.

(38) Rani, A.; Venkatesu, P. Insights into the Interactions between Enzyme and Co-Solvents: Stability and Activity of Stem Bromelain. *Int. J. Biol. Macromol.* **2015**, *73*, 189−201.

(39) Kinney, J. N.; Salmeen, A.; Cai, F.; Kerfeld, C. A. Elucidating Essential Role of Conserved Carboxysomal Protein CcmN Reveals Common Feature of Bacterial Microcompartment Assembly. *J. Biol. Chem.* **2012**, *287* (21), 17729−17736.

(40) Juodeikis, R.; Lee, M. J.; Mayer, M.; Mantell, J.; Brown, I. R.; Verkade, P.; Woolfson, D. N.; Prentice, M. B.; Frank, S.; Warren, M. J. Effect of Metabolosome Encapsulation Peptides on Enzyme Activity, Coaggregation, Incorporation, and Bacterial Microcompartment Formation. *Microbiologyopen* **2020**, *9* (5), No. e1010.

(41) Aussignargues, C.; Paasch, B. C.; Gonzalez-Esquer, R.; Erbilgin, O.; Kerfeld, C. A. Bacterial Microcompartment Assembly: The Key Role of Encapsulation Peptides. *Commun. Integr. Biol* **2015**, *8* (3), No. e1039755.

(42) Fan, C.; Cheng, S.; Liu, Y.; Escobar, C. M.; Crowley, C. S.; Jefferson, R. E.; Yeates, T. O.; Bobik, T. A. Short N-Terminal Sequences Package Proteins into Bacterial Microcompartments. *Proc. Natl. Acad. Sci. U.S.A.* **2010**, *107* (16), 7509−7514.

(43) Jakobson, C. M.; Slininger Lee, M. F.; Tullman-Ercek, D. De Novo Design of Signal Sequences to Localize Cargo to the 1,2-propanediol Utilization Microcompartment. *Protein Sci.* **2017**, *26* (5), 1086−1092.

(44) Tefft, N. M.; Wang, Y.; Jussupow, A.; Feig, M.; TerAvest, M. A. Controlled Enzyme Cargo Loading in Engineered Bacterial Microcompartment Shells. *Biochemistry* **2025**, *64* (6), 1285−1292.

(45) Faulkner, M.; Szabó, I.; Weetman, S. L.; Sicard, F.; Huber, R. G.; Bond, P. J.; Rosta, E.; Liu, L.-N. Molecular Simulations Unravel the Molecular Principles That Mediate Selective Permeability of Carboxysome Shell Protein. *Sci. Rep.* **2020**, *10* (1), 17501.

(46) Mahinthichaichan, P.; Morris, D. M.; Wang, Y.; Jensen, G. J.; Tajkhorshid, E. Selective Permeability of Carboxysome Shell Pores to Anionic Molecules. *J. Phys. Chem. B* **2018**, *122* (39), 9110−9118.

(47) Sarkar, D.; Maffeo, C.; Sutter, M.; Aksimentiev, A.; Kerfeld, C.; Vermaas, J. Atomic View of Photosynthetic Metabolite Permeability Pathways and Confinement in Cyanobacterial Carboxysomes. *ChemRxiv* **2024**, *12*..

(48) Chowdhury, C.; Chun, S.; Pang, A.; Sawaya, M. R.; Sinha, S.; Yeates, T. O.; Bobik, T. A. Selective Molecular Transport through the Protein Shell of a Bacterial Microcompartment Organelle. *Proc. Natl. Acad. Sci. U.S.A.* **2015**, *112* (10), 2990−2995.

(49) Cai, F.; Sutter, M.; Bernstein, S. L.; Kinney, J. N.; Kerfeld, C. A. Engineering Bacterial Microcompartment Shells: Chimeric Shell Proteins and Chimeric Carboxysome Shells. *ACS Synth. Biol.* **2015**, *4* (4), 444−453.

(50) Aussignargues, C.; Pandelia, M.-E.; Sutter, M.; Plegaria, J. S.; Zarzycki, J.; Turmo, A.; Huang, J.; Ducat, D. C.; Hegg, E. L.; Gibney, B. R.; Kerfeld, C. A. Structure and Function of a Bacterial Microcompartment Shell Protein Engineered to Bind a [4Fe-4S] Cluster. *J. Am. Chem. Soc.* **2016**, *138* (16), 5262−5270.

(51) Slininger Lee, M. F.; Jakobson, C. M.; Tullman-Ercek, D. Evidence for Improved Encapsulated Pathway Behavior in a Bacterial Microcompartment through Shell Protein Engineering. *ACS Synth. Biol.* **2017**, *6* (10), 1880−1891.

(52) Range, K. L.; Chiang, T. K.; Pramanik, A.; Landa, J. F.; Snyder, S. N.; Zuo, X.; Tiede, D. M.; Utschig, L. M.; Hegg, E. L.; Sutter, M.; Kerfeld, C. A.; Ralston, C. Y. A Chaotrope-Based Approach for Rapid in Vitro Assembly and Loading of Bacterial Microcompartment Shells. *bioRxiv* **2024**, *1*, 621445.

https://doi.org/10.1021/acsnano.4c15538